



Cite this: *Chem. Sci.*, 2025, 16, 16841 All publication charges for this article have been paid for by the Royal Society of ChemistryReceived 9th June 2025  
Accepted 11th August 2025

DOI: 10.1039/d5sc04193g

rsc.li/chemical-science

# Improving the optical nonlinearity of covalent organic frameworks through spatial electron transport channels within the pore environment

Kangshuai Geng, Yi Wei, Yupei Sun, Jing Huang, Jie Wu \* and Hongwei Hou \*

The influence of spatial electron transport channels in covalent organic frameworks (COFs) on third-order nonlinear optical (NLO) performance remains largely unknown. Herein, we present a method for preparing host–guest (H–G) COF composites with diverse pore environments to investigate their NLO performance. Pt nanoparticles (NPs) were selected as guests and confined into two novel azo/ethylene-decorated highly crystalline Azo-COF and Et-COF. The synthesized Pt NPs@Azo-COF and Pt NPs@Et-COF exhibit better NLO performance than Azo-COF and Et-COF under laser irradiation in the near-infrared to the visible range. In the near-infrared range (1064 nm), the reverse saturable absorption (RSA) of Pt NPs@Azo-COF and Pt NPs@Et-COF has increased by 4.62-fold and 3.25-fold, respectively, and the corresponding self-defocusing properties have also increased by 3.01-fold and 2.17-fold. Moreover, with the confinement of Pt NPs, the NLO absorption of Azo-COF and Et-COF changed from saturable absorption (SA) to RSA in the visible range (532 nm). Theoretical calculations and transient absorption demonstrate that the superior NLO performance of Pt NPs@Azo-COF is attributed to the reduction of the band-filling effect of excited states caused by the charge transfer between Pt NPs and Azo-COF, thereby optimizing the absorption cross-section of the ground state and excited state. This study expands the application range of COFs in the NLO field and opens a new avenue for improving NLO properties by modulating the pore environment.

## Introduction

Covalent organic frameworks (COFs) have attracted widespread attention due to their controllable structure, strong covalent bonds, well-defined molecular arrangement, and excellent stability.<sup>1</sup> These advantages enable the versatile COFs to have exceptional gas adsorption,<sup>2</sup> catalysis,<sup>3</sup> and optoelectronic properties.<sup>4</sup> With the continuous deepening of performance research, COFs have gradually emerged in third-order nonlinear optics (NLO) owing to their wide linear absorption band and low electronic transition energy.<sup>5</sup> To date, developing COFs with excellent NLO performance has primarily focused on constructing efficient electron transport channels.<sup>6</sup> On the one hand, designing diverse building blocks can allow COF skeletons to generate specific donor–acceptor electron transport channels, thus increasing the distribution range of the electron cloud.<sup>7</sup> On the other hand, choosing the appropriate linkages can directionally regulate the direction of electron transport channels, thereby promoting the overlap of electronic wave functions.<sup>8</sup> However, these studies concentrate on regulating electron transport channels within the COF skeleton, and the influence of the pore environment, which serves as a natural

spatial electron transport channel, on NLO performance has not been investigated.

Establishing spatial electron transport channels requires the confinement of guest molecules into the pore environment, forming host–guest (H–G) COF composites.<sup>9</sup> Among numerous guest molecules, metal nanoparticles (NPs) have attracted our attention due to their unique electronic structures, uniform adjustable sizes, and excellent NLO performance.<sup>10</sup> The quantum effect results in the various properties being greatly dependent on the size dimension of metal NPs. When the size is reduced, the higher surface energy often accompanies migratory aggregation, which comes at the cost of performance.<sup>11</sup> The pore environment of COFs with physical and chemical confinement effects can effectively avoid the migratory aggregation of metal NPs, and the geometric and electronic structures of metal NPs would be significantly affected by H–G interactions with the COF skeleton.<sup>12</sup> The surface plasmon resonance of confined metal NPs can improve near-field enhancement effects and exhibit strong light absorption and scattering behavior, which is fed back to the COF skeleton through H–G interactions, modulating the electronic structure of COFs.<sup>13</sup> Therefore, designing metal NPs@COFs is an effective strategy for developing excellent H–G COF composites, which can not only integrate the advantages of COFs and metal NPs

College of Chemistry, Zhengzhou University, Zhengzhou, Henan, 450001, P. R. China.  
E-mail: wujie@zzu.edu.cn; houghongw@zzu.edu.cn



but also investigate the effect of spatial electron transport channels on third-order NLO performance.

Herein, Pt NPs were successfully confined into two novel N=N and C=C decorated Azo-COF and Et-COF with hexagonal honeycomb mesoporous structures, forming Pt NPs@Azo-COF and Pt NPs@Et-COF. As expected, NLO results show Pt NPs@Azo-COF and Pt NPs@Et-COF exhibit better reverse saturable absorption (RSA) effects and self-defocusing properties than Azo-COF and Et-COF under 1064 nm laser excitation. Interestingly, with the confinement of Pt NPs, the NLO absorption of Azo-COF and Et-COF can be altered from saturable absorption (SA) to RSA under 532 nm laser irradiation. Theoretical calculation and transient absorption indicated that the superior NLO performance of Pt NPs@Azo-COF was due to the optimized absorption cross-section of the excited state and ground state and improved electronic structure caused by electron transfer between Pt NPs and Azo-COF. The study offers a strategy for understanding the importance of spatial electron transport channels in the third-order NLO performance.

## Results and discussion

### Design and synthesis of Pt NPs@Azo-COF and Pt NPs@Et-COF

To achieve the confinement of metal NPs, the pore size and skeleton binding site are two important factors that influence the selection of COFs. On the one hand, the pore environment of mesoporous COFs can provide more effective interaction between COFs and high-intensity light fields and sufficient space to accommodate metal NPs.<sup>14</sup> On the other hand, due to the stronger binding ability of metal NPs to N atomic sites, increasing the N atoms of the skeleton can promote the confinement of metal NPs.<sup>15</sup> This strategy allows Pt NPs to be dispersed in an orderly manner into the pore environment of COFs and avoids the aggregation of Pt NPs. Herein, the hexagonal honeycomb COFs of  $[C_3 + C_2]$  combination usually have a large pore size, and two different types of building blocks with rigid aromatic rings are required to meet the spatial guidance of bond connection and backbone propagation.<sup>16</sup> Diphenylene and azobenzene with inherent NLO performance may be the reasonable choice for  $C_2$  building blocks, which not only meet the requirements of skeleton rigidity but also verify the role of the N atoms. Two mesoporous COFs (Azo-COF and Et-COF) with highly crystalline hexagonal honeycomb structures were successfully designed and synthesized by the Schiff base

condensation reaction (Fig. 1). Pt NPs with excellent photoelectric and NLO properties were introduced into the COF pores through the ship-in-bottle strategy.<sup>17</sup> Specifically,  $K_2PtCl_6$  was introduced into the COF pores followed by reduction to construct Pt NPs@Azo-COF and Pt NPs@Et-COF. In the process,  $[PtCl_6]^{2-}$  is hydrolyzed into  $[PtCl_4(H_2O)_2]$  in an aqueous solution,<sup>18</sup> and the N atoms on the COF pore wall are beneficial to the combination of  $[PtCl_4(H_2O)_2]$  through hydrogen bonding and coordination interactions, and then treatment with  $NaBH_4$  to obtain confined Pt NPs (Fig. 1). Compared to C=C decorated Et-COF, the highly dispersed N=N in the Azo-COF can promote the confinement of Pt NPs in the pore environment, thereby providing a foundation for studying the diversified spatial electron transport channels.

### Characterization of Pt NPs@Azo-COF and Pt NPs@Et-COF

Azo-COF and Et-COF were synthesized *via* a Schiff-base condensation reaction of an imine bond (Fig. S1). The crystal-line feature of Azo-COF and Et-COF was confirmed from experimental and simulated powder X-ray diffraction (PXRD) patterns. As shown in Fig. 2a and b, the PXRD pattern of Azo-COF shows prominent diffraction peaks at  $2.32^\circ$  ( $2.34^\circ$  for Et-COF), which can be assigned to the (100) facets. The sharp and well-resolved diffraction peaks revealed that the 2D polymerization structure of Azo-COF and Et-COF exhibits intrinsic long-range orderliness. Pawley refinement was performed on experimental PXRD patterns of Azo-COF disclosing  $P6m$  space cell unit parameters of  $a = b = 48.6045 \text{ \AA}$ ,  $c = 3.44660 \text{ \AA}$ ,  $\alpha = \beta = 90^\circ$  and  $\gamma = 120^\circ$  with the residual factors of  $R_{wp} = 3.89\%$  and  $R_p = 3.08\%$ . The crystal model of Et-COF provides cells of the  $P6m$  space group,  $a = b = 49.0689 \text{ \AA}$ ,  $c = 3.4545 \text{ \AA}$ ,  $\alpha = \beta = 90^\circ$  and  $\gamma = 120^\circ$  with lower  $R$ -factors ( $R_{wp} = 3.22\%$  and  $R_p = 2.25\%$ ) by the Pawley refinement procedure. Refined PXRD patterns agree with the experimental data, as confirmed from the negligible difference curve. The type-IV sorption curves of Azo-COF and Et-COF observed in  $N_2$  adsorption-desorption isotherms revealed mesoporous characteristics (Fig. 2c). Pore size distribution evaluated using non-local density functional theory (NLDFT) reveals an average pore size of 2.97 and 2.86 nm for Azo-COF and Et-COF, respectively (Fig. S2). The micro-structure of Azo-COF and Et-COF was further studied using high-resolution transmission electron microscopy (HR-TEM), which is highly challenging for COFs since their structure is sensitive upon exposure to an electron beam.<sup>19</sup> As shown in Fig. 2d, Azo-COF reveals a long-range structural ordering of a hexagonal honeycomb lattice continuously distributed along the (001) direction. Sharp diffraction spots were observed in a hexagonal arrangement in the associated fast Fourier transform (FFT) pattern, further proving the high crystallinity. According to the simulation structures, the periodic dark spots are associated with the two building blocks, and the bright stripes correspond to pore apertures formed by the stacking of two-dimensional layers in the lattice. Notably, Azo-COF also exhibits distinct lattice fringes with a spacing of 3.06 nm, which are attributed to the (100) plane of pore size (Fig. 2f). The slight inconsistency in pore size results between TEM and  $N_2$

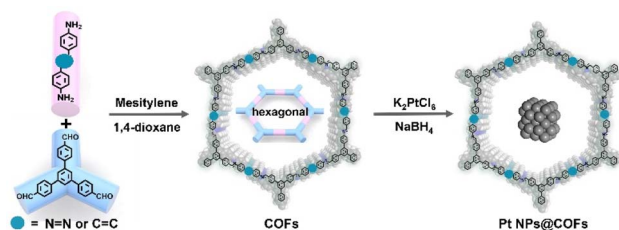
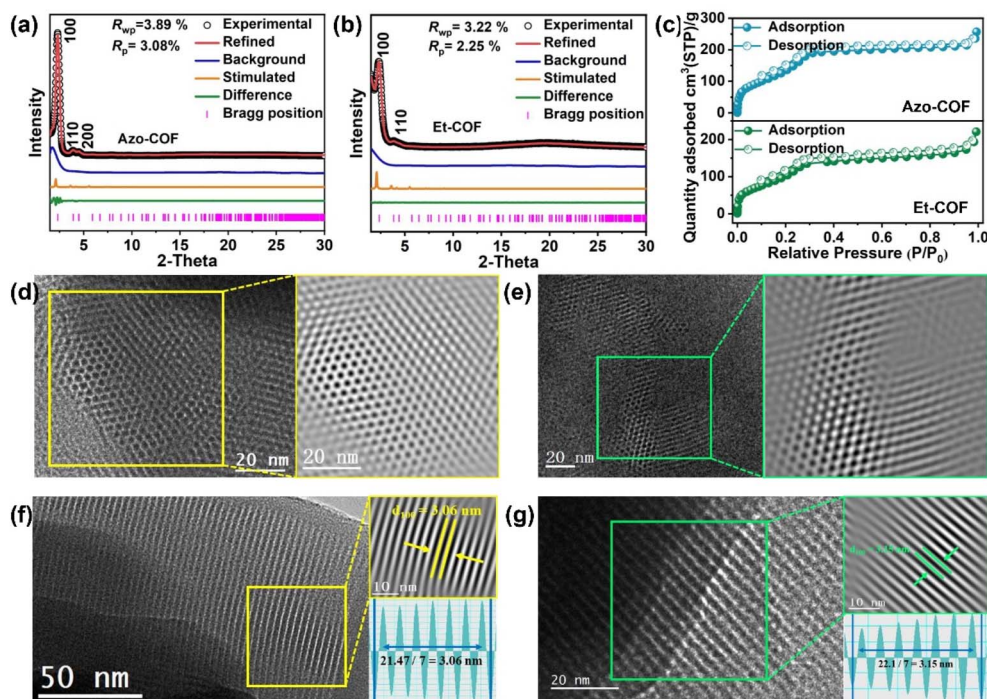


Fig. 1 Scheme of the synthesis of Pt NPs@Azo-COF and Pt NPs@Et-COF.





**Fig. 2** Experimental and simulated PXRD patterns and structure models along the [100] and [001] directions (insets) of (a) Azo-COF and (b) Et-COF. (c) N<sub>2</sub> adsorption-desorption isotherms of Azo-COF and Et-COF. HR-TEM images of (d) Azo-COF and (e) Et-COF. Right: enlarged images of a selected area showing well-ordered hexagonal honeycomb lattice fringes, (f) Azo-COF, (g) Et-COF. Top right: enlarged images of a selected area showing well-ordered strip lattice fringes. Bottom right: Fast Fourier Transform (FFT) pattern.

absorption is attributed to different sample preparation methods and testing principles. Correspondingly, the HR-TEM also shows that Et-COF has a clear hexagonal honeycomb lattice and strip lattice fringes with a spacing of 3.15 nm (Fig. 2e and g). Thermogravimetric (TG) curves (Fig. S3) show that Azo-COF begins to lose weight at 131 °C, attributed to the release of solvent molecules from the surface and cavities. As the temperature increased to 411 °C, the Azo-COF skeleton collapsed. Et-COF showed a similar weight loss trend and skeleton collapse temperature. Compared to N=N decorated Azo-COF without residual mass, C=C decorated Et-COF has a residual mass of 7.3%, which may be due to the higher C content.

Pt NPs@Azo-COF and Pt NPs@Et-COF were prepared through the ship-in-bottle strategy.<sup>20</sup> HR-TEM images (Fig. 3a–c) of Pt NPs@Azo-COF show that Pt NPs were uniformly distributed on COFs. The Pt NPs possessed an average diameter of 2.8 nm, which matches the size of the pores well. The lattice spacing of 0.21 nm is attributed to the (111) plane of Pt, and EDS mapping (Fig. 3d) of Pt NPs@Azo-COF proved the existence of the Pt element in the Azo-COF support. But, the HR-TEM images (Fig. S4) of Pt NPs@Et-COF show that Pt NPs have poor dispersibility and low content, which may be attributed to the fewer N active sites that are not conducive to the confinement of ultrasmall Pt NPs. To further expand the variety of H-G COF composites, we also prepared Azo-COF and Et-COF loaded with Au NPs and Ag NPs. HR-TEM images (Fig. S5) of Au NPs@Azo-COF show that Au NPs possessed an average diameter

of 3.2 nm. The HR-TEM images (Fig. S6) of Au NPs@Et-COF show that Au NPs have poor dispersibility, which further verifies that the N active sites are conducive to promoting the confinement of metal NPs. However, HR-TEM images (Fig. S7 and S8) of Ag NPs@Azo-COF and Ag NPs@Et-COF show that the size of Ag NPs is significantly larger, which is severely mismatched with the pore size of Azo-COF and Et-COF. The large size of Ag NPs may be attributed to the highly reducible nature under photothermal conditions and the higher reduction potential, which leads to the excessive growth of Ag NPs.

The PXRD of Pt NPs@Azo-COF and Pt NPs@Et-COF (Fig. 3e and S9) shows an intense (100) reflection at  $2\theta = 2.32^\circ$  and  $2\theta = 2.34^\circ$ , which is consistent with the characteristic diffraction peak of Azo-COF and Et-COF. This means that after the introduction of Pt NPs, the structural integrity of Azo-COF and Et-COF was preserved. In scanning electron microscopy (SEM) images, Azo-COF exhibits a micrometer scale date pitted morphology, while Et-COF shows an agglomerated bulk morphology (Fig. S10). The C, N, and O elements are uniformly distributed according to the mapping image. With the introduction of Pt NPs into Azo-COF and Et-COF, although there was a slight change in morphology, Pt NPs did not produce significant deposition on the surface (Fig. S11). N<sub>2</sub> adsorption-desorption isotherms (Fig. 3f and S12) show the introduction of Pt NPs does not affect the type of adsorption curve. But, BET surface areas of Pt NPs@Azo-COF ( $66.315 \text{ m}^2 \text{ g}^{-1}$ ) and Pt NPs@Et-COF ( $90.70 \text{ m}^2 \text{ g}^{-1}$ ) are lower than those of Azo-COF ( $394.77 \text{ m}^2 \text{ g}^{-1}$ ) and Et-COF ( $288.63 \text{ m}^2 \text{ g}^{-1}$ ), respectively,





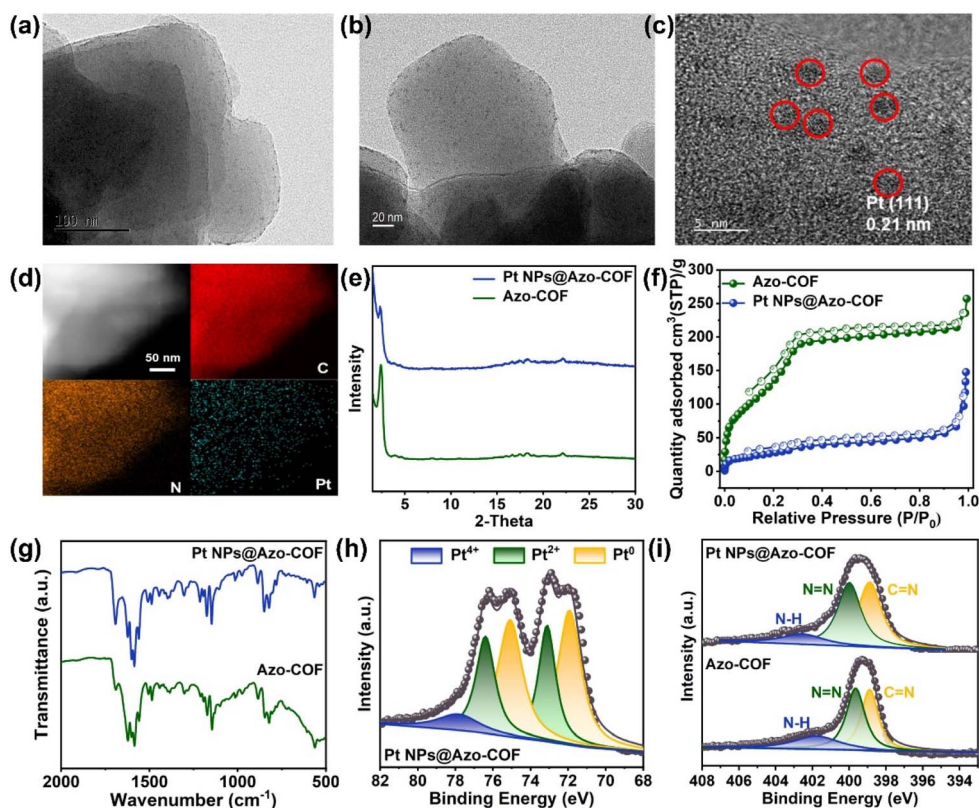


Fig. 3 Structural characterization of Pt NPs@Azo-COF. (a–c) HR-TEM images. (d) EDS mapping of C, N, and Pt elements. (e) PXRD patterns. (f)  $\text{N}_2$  adsorption–desorption isotherms. (g) FT-IR spectra. (h) High-resolution Pt 4f XPS spectra. (i) N 1s XPS spectra.

which is attributed to the occupation of the COFs pore environment by Pt NPs. The unchanged pore size confirms that the structures of Azo-COF and Et-COF remain intact after the introduction of Pt NPs (Fig. S13). In the Fourier transform infrared spectra (FT-IR, Fig. S14) of Azo-COF and Et-COF, the characteristic peaks of  $\text{C}=\text{O}$  ( $1685\text{ cm}^{-1}$ ) stretching vibration and  $\text{NH}_2$  ( $3373\text{ cm}^{-1}$ ) disappeared, and a new characteristic peak  $\text{C}=\text{N}$  ( $1622\text{ cm}^{-1}$ ) appeared, indicating that the imine linkage COFs were successfully prepared. The characteristic stretching bands of  $\text{N}=\text{N}$  and  $\text{C}=\text{C}$  appeared at  $1506\text{ cm}^{-1}$  and  $1514\text{ cm}^{-1}$ , indicating that Azo-COF and Et-COF contain stable azobenzene and stilbene moieties. The FT-IR spectrum of Pt NPs@Azo-COF and Pt NPs@Et-COF (Fig. 3g and S15) was consistent with the pattern of Azo-COF and Et-COF, suggesting no destruction of the  $\text{C}=\text{N}$  bond after the introduction of Pt NPs into Azo-COF and Et-COF. The  $^{13}\text{C}$  NMR spectra (Fig. S16) further indicated the formation of the  $\text{C}=\text{N}$  by the presence of the peak at  $\sim 161\text{ ppm}$ .

To explore why the  $\text{N}=\text{N}$  bond was conducive to Pt NPs anchoring and dispersion, XPS analysis was employed to investigate the chemical states and elemental compositions of Pt NPs@Azo-COF and Pt NPs@Et-COF. In the Pt 4f XPS spectra (Fig. 3h), the split spin-orbit peaks are attributed to the Pt  $4f_{7/2}$  and  $4f_{5/2}$  orbitals. For Pt NPs@Et-COF (Fig. S17), the binding energies at  $71.9$  and  $75.3\text{ eV}$  correspond to  $\text{Pt}^0$ , and the peaks at  $73.2$  and  $76.4\text{ eV}$  are associated with the oxidation state of  $\text{Pt}^{2+}$ .<sup>21</sup> Compared to Pt NPs@Et-COF, the Pt 4f XPS spectrum of Pt

NPs@Azo-COF shows peaks shifted to lower binding energies; the peaks of metallic Pt ( $\text{Pt}^0$ ) changed to  $71.7$  and  $75.1\text{ eV}$ , and those of  $\text{Pt}^{2+}$  moved to  $73.0$  and  $76.0\text{ eV}$ .<sup>22</sup> This shift illustrated that Pt in Pt NPs@Azo-COF is in an electron-rich state and the electronic state could be altered *via* electron donation by electronegative N atoms. In addition, the  $77.7\text{ eV}$  of  $\text{Pt}^{4+}$  in Pt NPs@Azo-COF can be observed, proving the strong binding effect of the N sites to  $[\text{PtCl}_4(\text{H}_2\text{O})_2]$ . The assumption was further confirmed from the N 1s XPS spectrum of Pt NPs@Azo-COF, shown in Fig. 3i. The peak of  $\text{N}=\text{N}$  in Pt NPs@Azo-COF shifted to higher binding energies ( $400.1\text{ eV}$ ) compared to Azo-COF ( $399.6\text{ eV}$ ). Furthermore, the peak area of  $\text{Pt}^0$  in Pt NPs@Azo-COF was much larger than that in Pt NPs@Et-COF, which illustrated that Pt NPs@Azo-COF contained more metallic Pt than Pt NPs@Et-COF. These results show that the N sites of  $\text{N}=\text{N}$  are conducive to the interaction with  $[\text{PtCl}_4(\text{H}_2\text{O})_2]$ .

To gain insight into the relationship between the micro-structure and the NLO properties, the photophysical properties and band gap structure were characterized using solid-state UV-vis diffuse reflection spectroscopy. The absorption band edges of Azo-COF and Et-COF are located at  $587$  and  $566\text{ nm}$ , respectively, with well-visible absorption and a wide absorption band (Fig. S18). Pt NPs@Azo-COF and Pt NPs@Et-COF displayed an obvious bathochromic shift phenomenon, and the confined Pt NPs can largely extend the absorption spectrum (Fig. S19), indicating a high enhancement of light harvesting



and charge transfer interaction between the COFs and Pt NPs. As shown in Fig. S20 and S21, according to the transformed Kubelka–Munk function,<sup>23</sup> the optical band gap ( $E_g$ ) values of Azo-COF and Et-COF are 2.17 and 2.31 eV, respectively, while those of Pt NPs@Azo-COF and Pt NPs@Et-COF are 1.98 and 2.22 eV, respectively. Thus, introducing Pt NPs into the pore environment of COFs is conducive to optimizing the bandgap structure.

Atomic absorption was tested to obtain the exact content of Pt NPs in COFs. The Pt NP loading content in Pt NPs@Azo-COF and Pt NPs@Et-COF is 0.84% and 0.47%, respectively. To understand the effect of Pt loading content on NLO performance, we further prepared Azo-COF with a Pt loading of 0.65 wt% and 1.12 wt% by altering the concentration of  $K_2PtCl_6$  in the precursor solution. HR-TEM images (Fig. S22 and S23) of 0.65 wt% Pt NPs@Azo-COF and 1.12 wt% Pt NPs@Azo-COF showed that Pt NPs can still be evenly distributed on Azo-COF. With the Pt loading content increasing, the size of the NPs significantly expands. The average diameter of Pt NPs is 2.5 nm in 0.65 wt% Pt NPs@Azo-COF, while it is 3.0 nm in 1.12 wt% Pt NPs@Azo-COF. The bandgap structure (Fig. S24) exhibits a dependency on the Pt loading content. As the Pt loading content increases, the absorption band gradually shifts towards the longer wavelength, and the  $E_g$  value decreases.

### Third-order NLO properties under 1064 nm laser irradiation

The efficient  $\pi$ -conjugation and unique interlayer stacking of COFs endow them with excellent photoelectron properties conducive to generating third-order NLO behavior. The NLO absorption of Azo-COF exhibits valley-shaped curves (Fig. 4a), indicating typical reverse saturation absorption (RSA) behavior.

The nonlinear absorption coefficient ( $\beta$ ) of Azo-COF was calculated to be  $2.24 \times 10^{-10} \text{ m W}^{-1}$  (Table S1). Due to the wavelength of 1064 nm being located in the non-resonance region, the NLO absorption process is more derived from virtual transitions and occurs rapidly.<sup>24</sup> The  $E_g$  value of Azo-COF is 2.17 eV, significantly greater than the single photoenergy (1.17 eV) and less than the two-photoenergy (2.34 eV) of 1064 nm. Therefore, under 1064 nm laser irradiation, Azo-COF does not produce actual electron transitions but may undergo a two-photon-induced excited-state absorption process, resulting in Azo-COF exhibiting RSA behavior. Based on the electron and charge distribution (see the SI for a detailed discussion), the electrons of Azo-COF prefer to move around the  $N=N$  and  $C=N$ . The connecting bond in COFs can be precisely replaced from  $N=N$  to  $C=C$ , which helps understand the influence of different connecting bonds on NLO properties. Et-COF also exhibited similar RSA behavior (Fig. 4a), and the corresponding  $\beta$  value was  $1.67 \times 10^{-10} \text{ m W}^{-1}$  (Table S1), which was smaller than that of Azo-COF. Compared to Et-COF, Azo-COF has a greater electron cloud overlap on the HOMO and LUMO, and the electrons are more likely to undergo local electron excitation. In ESP analysis, there is more charge distribution around  $N=N$  than  $C=C$ , which may be attributed to  $n$  electrons on  $p$  orbitals. Thus, the well-defined  $N=N$  in frameworks can finely tune the band gap and electronic structures of COFs.

The NLO refraction (Fig. 4b) shows that as the COFs move from  $-Z$  to  $+Z$ , the normalized transmittance line first increases and then decreases, forming an asymmetric peak-valley shape curve. Near the beam waist, the increase in laser intensity is accompanied by sharp changes in the NLO refractive index. In contrast, the laser intensity changes slowly away from the beam waist, causing a minimal change in the NLO refractive index.<sup>25</sup>

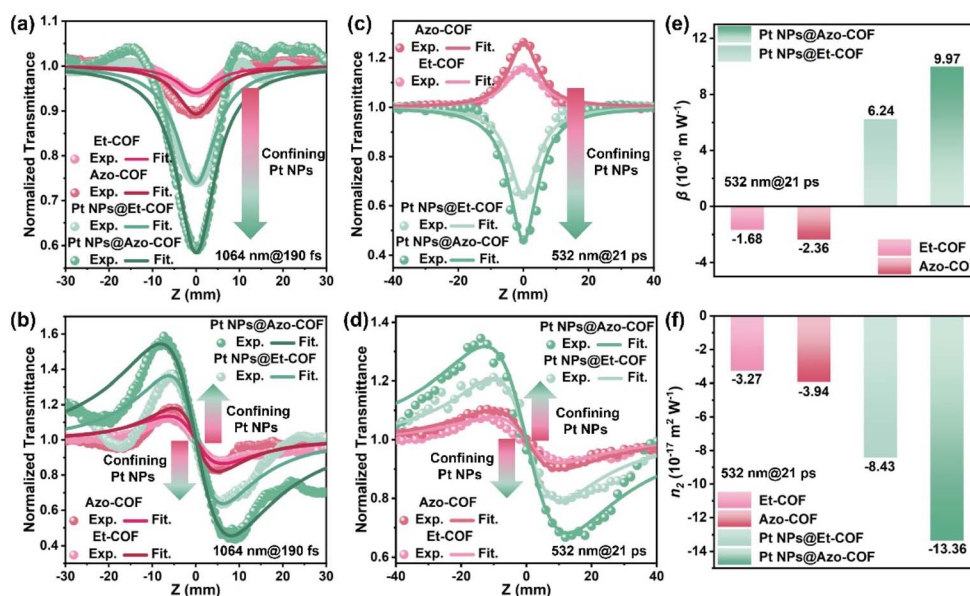


Fig. 4 Third-order NLO properties of Et-COF, Azo-COF, Pt NPs@Et-COF, and Pt NPs@Azo-COF. Normalized open-aperture Z-scan curves (a) under 1064 nm laser irradiation. (c) Under 532 nm laser irradiation. Normalized close-aperture Z-scan curves (b) under 1064 nm laser irradiation. (d) Under 532 nm laser irradiation. (e) Nonlinear absorption coefficient and (f) nonlinear refractive index under 532 nm laser irradiation. The measured and fitted results are shown by data points and solid lines, respectively.



This phenomenon is attributed to the uneven radial distribution of the refractive index caused by the Gaussian transverse. Azo-COF and Et-COF act as concave lenses in the optical path, inducing a self-defocusing phenomenon and negative nonlinear refraction index ( $n_2$ ). Due to the use of a pulsed laser in this experiment, the primary response of NLO refractive behavior is the electron Kerr effect.<sup>26</sup> The  $n_2$  values of Azo-COF and Et-COF calculated are  $-8.13 \times 10^{-17} \text{ m}^2 \text{ W}^{-1}$  and  $-7.31 \times 10^{-17} \text{ m}^2 \text{ W}^{-1}$  (Table S1). Combined with frontier molecular orbital and ESP analysis, the difference in NLO refractive performance may be attributed to the transport of  $\pi$  electrons of the N=N bond, effectively increasing the electron density in the COF skeleton and allowing more electrons to participate in the transport process, resulting in stronger self-defocusing performance.

Small-sized Pt NPs can generate excellent NLO properties through plasma effects, quantum size characteristics, and multi-mechanism synergistic effects.<sup>27</sup> However, smaller Pt NPs are more unstable and tend to aggregate. According to the characterization of Pt NPs@Et-COF and Pt NPs@Azo-COF, the unique pore environment of Azo-COF and Et-COF can restrain the aggregation and exert size effects of Pt NPs, and Pt NPs can adjust the physicochemical properties of COFs by H-G interaction, thereby optimizing the electronic structure and distribution of the independent material.<sup>28</sup> The NLO properties of Pt NPs@Azo-COF in the non-resonant region were tested to investigate the role of spatial electron transport channels in NLO performance. Compared with the NLO absorption of Azo-COF, that of Pt NPs@Azo-COF (Fig. 4a) maintains a valley-shaped curve, but the valley value increases. The  $\beta_{\text{eff}}$  values of Pt NPs@Azo-COF have increased 4.62 times, with a specific value of  $10.36 \times 10^{-10} \text{ m W}^{-1}$ . For NLO refraction, with the confinement of Pt NPs, the severe rearrangement of electron cloud distribution disrupts the Kerr refraction effect, resulting in the peak-valley value of Pt NPs@Azo-COF being significantly larger than that of Azo-COF (Fig. 4b). The  $n_2$  values have increased 3.01 times, with a specific value of  $-24.26 \times 10^{-17} \text{ m}^2 \text{ W}^{-1}$ . When the laser irradiates Pt NPs@Azo-COF, Azo-COF can undergo energy exchange with confined Pt NPs through H-G interaction, optimizing the electron cloud distribution and polarization fields.

To verify the importance of spatial electron transport channels, we also investigated the NLO performance of Pt NPs@Et-COF. Compared to Et-COF, the NLO absorption of Pt NPs@Et-COF (Fig. 4a) shows that the valley value of the normalized transmittance is markedly enhanced, and the  $\beta_{\text{eff}}$  values increased 3.25 times, with a specific value of  $5.43 \times 10^{-10} \text{ m W}^{-1}$ . For NLO refraction (Fig. 4b), the peak-valley curve intensity has improved, and the  $n_2$  values increased 2.17 times, with a specific value of  $-15.89 \times 10^{-17} \text{ m}^2 \text{ W}^{-1}$ . Thus, confining Pt NPs into the pore environment of COFs is a way to improve NLO performance. To demonstrate the establishment of the spatial electron transfer channel, we tested the electrochemical impedance spectroscopy (EIS) and photocurrent response (Fig. S25). The semicircle of the Nyquist curve of Pt NPs@Azo-COF is smaller than that of Azo-COF, indicating that the impedance decreases after confining Pt

NPs into Azo-COF. The instantaneous current response of Pt NPs@Azo-COF is greater than that of Azo-COF, reflecting that the Pt NPs@Azo-COF has stronger charge transfer and photo-response abilities. Since the interaction and binding ability between COFs and Pt NPs can be effectively improved by changing the connecting bond types, N=N decorated Azo-COF with abundant N-atom sites promotes the confinement of Pt NPs. When Pt NPs are confined to Azo-COF, more N active sites are beneficial for establishing faster spatial electronic transport channels and exerting the  $\pi$  electron-facilitated NLO effect. NLO results show that the  $\beta_{\text{eff}}$  values and  $n_2$  values of Pt NPs@Azo-COF are both greater than those of Pt NPs@Et-COF in the non-resonant region. The enhanced NLO performance of Pt NPs@Azo-COF proves that the modulation of connecting bonds can also effectively improve the NLO performance of H-G COF composites.

### Third-order NLO properties under 532 nm laser irradiation

Generally, the third-order NLO process can be divided into two categories: non-resonant and resonant.<sup>29</sup> Since the resonance region usually has higher energy to excite electrons, COFs and Pt NPs@COFs may exhibit different NLO properties. Herein, we also studied the NLO performance in the resonant region (532 nm laser irradiation) to provide a more convincing explanation.<sup>30</sup> The NLO absorption behavior of Azo-COF and Et-COF (Fig. 4c) shows that the normalized transmittance increases continuously as the sample moves to the focal position, exhibiting a typical saturable absorption (SA) phenomenon, which is contrary to the RSA behavior in the non-resonance region (1064 nm laser irradiation). Under the irradiation of a 1064 nm laser, electrons of Azo-COF and Et-COF will generate multiphoton absorption and transition to excited states. Due to the denser arrangement of excited state energy levels and the lower photon energy required for higher transitions, electrons will preferentially undergo excited state absorption processes compared to ground state transitions, which is beneficial for exhibiting RSA behavior. Under the irradiation of a 532 nm laser, when the electron transitions from the ground state to the excited state, the excited state electron cannot relax to the ground state in time, resulting in a decrease in ground state absorption, which helps to produce SA behavior. The calculated  $\beta$  value of Azo-COF is  $-2.36 \times 10^{-10} \text{ m W}^{-1}$ , and that of Et-COF is  $-1.68 \times 10^{-10} \text{ m W}^{-1}$ , further proving the importance of N=N connecting bonds for NLO absorption performance. Moreover, the SA performance under steady-state conditions (Fig. S26) enhances gradually with the increase in pulse energy, which can be explained by the Pauli-blocking effect.<sup>31</sup> As shown in Fig. S27, the SA performance of Azo-COF and Et-COF under dynamic-state conditions also shows a linear relationship as the pulse intensity increases, which was consistent with the results under steady-state conditions. For NLO refraction (Fig. 4d), with the change of connecting bonds, the increase in the instantaneous response capability of bound electrons leads to the peak-valley value of Azo-COF being significantly larger than that of Et-COF. The calculated  $n_2$  value of Azo-COF is  $-3.94 \times 10^{-17} \text{ m}^2 \text{ W}^{-1}$ , and that of Et-COF is  $-3.27 \times 10^{-17} \text{ m}^2 \text{ W}^{-1}$ .





To further confirm the importance of spatial electron transport channels, we also studied the NLO performance of Pt NPs@Et-COF and Pt NPs@Azo-COF. The NLO absorption behavior (Fig. 4c and S26) under different pulse energies shows that the normalized transmittance decreases continuously as the sample moves to the focal position, exhibiting a typical RSA phenomenon. The valley value of normalized transmittance enhances with the increase of pulse energy, indicating that Pt NPs@Et-COF and Pt NPs@Azo-COF exhibit pulse energy-dependent RSA behavior.<sup>32</sup> According to the corresponding fitting results (Table S1),  $\beta$  values of Pt NPs@Et-COF and Pt NPs@Azo-COF change with the variation of pulse energy, which may be attributed to the generation of high-order NLO absorption caused by two-photon-induced excited state absorption. In addition, with the introduction of Pt NPs, the NLO absorption performance (Fig. 4e) of Azo-COF and Et-COF can change from SA to RSA. When Pt NPs@Et-COF and Pt NPs@Azo-COF are excited using the laser, due to the presence of spatial electron transport channels between COFs and Pt NPs, the excited state electrons of COFs will relax to the energy level of Pt NPs, causing a deficit of electrons in the excited state of COFs. The deficit can contribute to the relaxation and transfer of excited state electrons in COFs and weaken the band-filling effect of excited state electrons.<sup>27</sup> The orbital vacancy of the excited state helps to improve the absorption cross-section of excited states and optimize the NLO absorption performance. For NLO refraction (Fig. 4d), with the confinement of Pt NPs, the spatial electron transport channels effectively improve the instantaneous electron response capability, resulting in a significant increase in the peak-valley value. The  $n_2$  values of Pt NPs@Et-COF and Pt NPs@Azo-COF increased by 2.57 and 3.39 times, with the specific value (Fig. 4f) of  $-8.43 \times 10^{-17} \text{ m}^2 \text{ W}^{-1}$  and  $-13.36 \times 10^{-17} \text{ m}^2 \text{ W}^{-1}$ , respectively. Furthermore, Pt NPs@Azo-COF also exhibited Pt loading-dependent NLO behavior (Fig. S28). The RSA properties of Pt NPs@Azo-COF gradually enhance as the Pt loading content increases. The  $\beta$  values (as shown in Table S1) of 0.65 wt% Pt NPs@Azo-COF increase from  $5.22 \times 10^{-10} \text{ m W}^{-1}$  to  $9.97 \times 10^{-10} \text{ m W}^{-1}$  for 0.84 wt% Pt NPs@Azo-COF,  $11.86 \times 10^{-10} \text{ m W}^{-1}$  for 1.12 wt% Pt NPs@Azo-COF. The trend change of NLO refractive performance is the same as that of NLO absorption properties. According to the fitting data, 1.12 wt% Pt NPs@Azo-COF has the best self-defocusing performance, with a value of  $-17.67 \times 10^{-17} \text{ m}^2 \text{ W}^{-1}$ . Therefore, regulating the pore environment of COFs can indeed effectively improve NLO performance.

The NLO properties of Au NPs@COFs and Ag NPs@COFs were tested to verify the influence of metal NPs on the NLO performance (Fig. S29). With the introduction of Au NPs into the pore environment of Azo-COF and Et-COF, the NLO absorption performance can change from SA to RSA, and the NLO refraction performance significantly enhances. The  $\beta$  values and  $n_2$  values (Table S1) of Au NPs@Azo-COF are  $8.36 \times 10^{-10} \text{ m W}^{-1}$  and  $-9.41 \times 10^{-17} \text{ m W}^{-2}$ , respectively, while those of Au NPs@Et-COF are  $5.59 \times 10^{-10} \text{ m W}^{-1}$  and  $-7.76 \times 10^{-17} \text{ m W}^{-2}$ , respectively. The NLO performance of Au NPs@Azo-COF is better than that of Au NPs@Et-COF, further

indicating that replacing connection bonds at the skeletal level can effectively improve NLO performance. Subsequently, we also investigated the NLO absorption and refractive properties of Ag NPs@Azo-COF and Ag NPs@Et-COF. Although the NLO absorption and refractive properties can also be improved after the introduction of Ag NPs into the pore environment, the NLO performance of Ag NPs@COFs is much lower than that of Pt NPs@COFs and Au NPs@COFs. The large size of Ag NPs makes it difficult to establish spatial electron transport channels within the pore environment, resulting in lower NLO performance of Ag NPs@COFs compared to Pt NPs@COFs and Au NPs@COFs. In addition, it is worth noting that the NLO performance of Pt NPs@COFs is superior to that of Au NPs@COFs. Compared to Au NPs, the smaller size of Pt NPs is more conducive to establishing spatial electron transport channels with COFs. Overall, these results indicate that the NLO performance level of metal NPs@COFs is highly dependent on the size of metal NPs.

### Third-order NLO electron excitation process

To explore the effect of N=N and C=C connecting bonds on NLO performance, theoretical calculations were performed for Azo-COF and Et-COF.<sup>33</sup> Tables S2 and S3 show the characteristics of the excited states calculated using time-dependent density functional theory, an extreme absorption band at 492.34 nm in Azo-COF. In Fig. S30, the electrons and holes in the excited state were not separated and almost completely overlapped (the centroid distance is 0.81 Å). The main distribution range was localized around C=N=N-C and C-C=N-C, indicating the transitions were mostly  $\pi-\pi^*$  and  $n-\pi^*$  local excitation, which dominates the NLO absorption properties of Azo-COF. For Et-COF, the strong excited state (489.34 nm, Fig. 5a) near 532 nm of Et-COF was selected. The electron-hole distributions on C-C=N-C are uniform and almost overlapping (the centroid distance is 0.82 Å), while that on C-C=C-C is separated and dominated by holes. This indicated that the NLO properties of Et-COF are influenced by both local excitation and charge transfer excitation. The corresponding hole-electron coulomb attractive energy ( $E_{\text{coul}}$ ) changes from 2.13 eV to 2.21 eV. Compared to Et-COF, Azo-COF effectively exerts  $n$  electron-facilitated  $n-\pi^*$  local excitation. To investigate the NLO absorption mechanism of Azo-COF and Et-COF, femto-second time-resolved transient absorption (fs-TA) spectroscopy was performed.<sup>34</sup> Pseudo-color images (Fig. 5b and c) show that Azo-COF exhibits a negative absorption signal range from 0.8 to 1.3 ps under the 532 nm detection wavelength. The results are consistent with SA properties in the resonance region, which may originate from a rapid ground-state bleaching process. In addition, Et-COF also has a negative transient absorption signal (Fig. S31), and the ground-state bleaching intensity is weaker than that of Azo-COF. To obtain the absorption cross-sectional areas of the ground and excited states, the transient absorption at 532 nm was tested (Fig. S32).<sup>35</sup> The values of  $\sigma_0$  and  $\sigma_1$  of Azo-COF are  $6.63 \times 10^{-22} \text{ cm}^2$  and  $4.84 \times 10^{-22} \text{ cm}^2$ , respectively. For Et-COF, data near the zero-delay time region give  $\sigma_0$  ( $5.76 \times 10^{-22} \text{ cm}^2$ )  $>$   $\sigma_1$  ( $5.03 \times 10^{-22} \text{ cm}^2$ ). The  $\sigma_0/\sigma_1$  of Et-COF (1.15) is



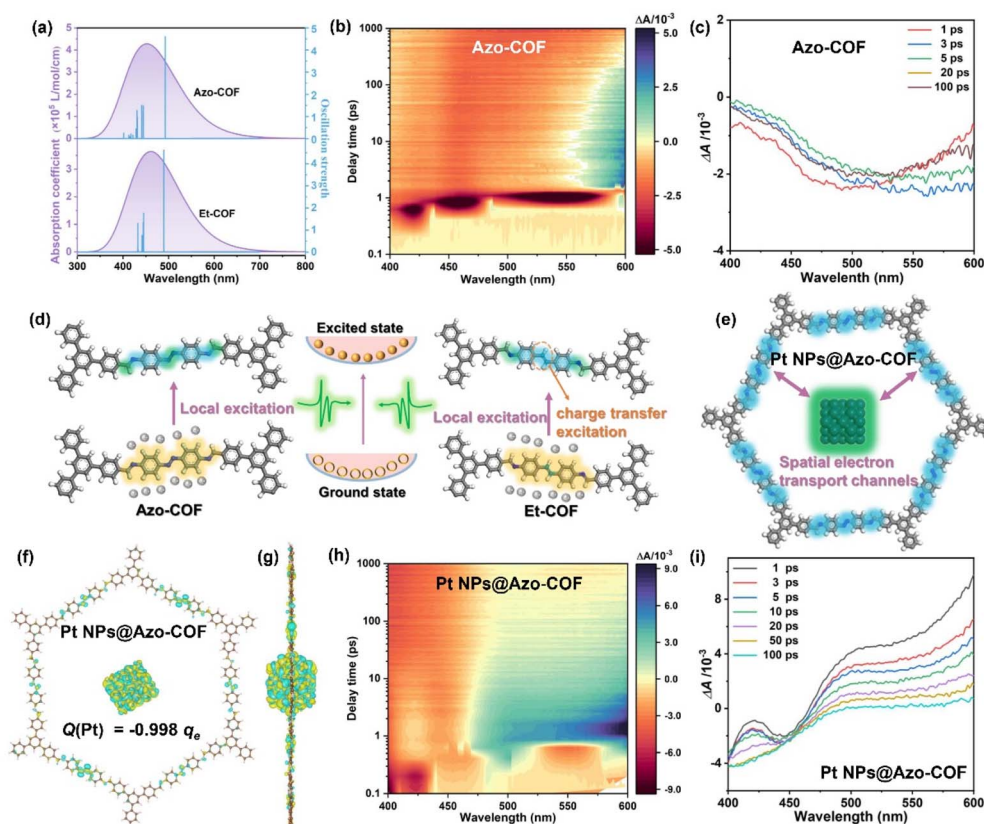


Fig. 5 (a) The calculated UV-vis absorption of Azo-COF and Et-COF models. (b) Pseudo-color images of fs-TA spectra for Azo-COF. (c) The fs-TA spectra at different decay times of Azo-COF. (d) Diagram of NLO absorption mechanisms of Azo-COF and Et-COF. (e) Diagram of NLO absorption mechanisms of Pt NPs@Azo-COFs. Charge density difference and Bader charge of Pt NPs@Azo-COF. (f) Top-view and (g) side-view. (h) Pseudo-color images of fs-TA spectra for Pt NPs@Azo-COF. (i) The fs-TA spectra at different decay times of Pt NPs@Azo-COF.

smaller than that of Azo-COF (1.36), which is beneficial for Azo-COF to exhibit better SA performance. Overall, the  $n$  electron-facilitated NLO effect (Fig. 5d) of Azo-COF is attributed to the stronger ground-state bleaching phenomenon caused by the connecting bond modulation.

Since the spatial electronic transport channels (Fig. 5e) are the important factor affecting the NLO absorption performance, we investigated the electron distribution and fs-TA spectroscopy of Pt NPs@Azo-COF. The charge density difference suggests that the interaction between Pt NPs and Azo-COF affected the charge distribution and formed a host-guest build-in electric field. Yellow and blue regions represent electron accumulation and depletion, respectively. In Fig. 5f and g, it can be concluded that there is a strong charge interaction ( $Q(\text{Pt}) = -0.998q_e$ , where  $q_e$  is the unit of charge transfer quantity). The electron distribution in the Azo-COF skeleton is mainly concentrated on the C=N and N=N bonds, and the electron dissipation at the N=N bond is more pronounced. Pt NPs in the Azo-COF pore environment exhibit strong electron enrichment ability, indicating that Azo-COF carries more negative charges while Pt NPs carry more positive charges, thereby constructing a spatial electron transport channel from Azo-COF to Pt NPs. The fs-TA spectra of Pt NPs@Azo-COF (Fig. 5h and i) have clear positive peaks at 480–600 nm, and the electrons mainly undergo the excited state

absorption process. With the prolongation of probe time, the TA intensity of Pt NPs@Azo-COF significantly weakened, attributed to the decrease of active photogenerated charge. By comparing the TA spectra of Azo-COF and Pt NPs@Azo-COF, the confinement of Pt NPs in the pore environment can convert ground-state bleaching to excited state absorption, consistent with NLO absorption changes. Under laser irradiation,  $\pi-\pi^*$  and  $n-\pi^*$  local excitation in the Azo-COF results in a significant reduction in band-filling effects of the excited state and exhibits SA behavior. After encapsulating Pt NPs, electrons of the excited state in the Azo-COF are transferred to the Pt NPs through spatial electron transport channels, effectively enhancing the ability of excited-state electrons to absorb photons and endowing Pt NPs@Azo-COF with excellent RSA performance. A similar excited state absorption range between 590 and 670 nm was observed after excitation in Pt NPs@Et-COF (Fig. S33). At 532 nm wavelength, the pumping fitting results (Fig. S34) of Pt NPs@Azo-COF are  $2.03 \times 10^{-21} \text{ cm}^2$  ( $\sigma_0$ ) and  $3.65 \times 10^{-21} \text{ cm}^2$  ( $\sigma_0$ ), while those of Pt NPs@Et-COF are  $1.43 \times 10^{-21} \text{ cm}^2$  ( $\sigma_0$ ) and  $1.89 \times 10^{-21} \text{ cm}^2$  ( $\sigma_1$ ). These results indicate that the presence of  $n$  electrons in N=N promotes spatial electron transfer and accelerates the transformation of charge states in the skeleton, resulting in the better NLO performance of Pt NPs@Azo-COF.





## Conclusions

In summary, we successfully introduced Pt NPs into the pore environment of Azo-COF and Et-COF, forming Pt NPs@Azo-COF and Pt NPs@Et-COF. With the confinement of Pt NPs, the NLO absorption and self-defocusing performance have significantly improved, which is attributed to establishing spatial electron transport channels between Azo-COF and Pt NPs. Theoretical calculations and transient absorption indicate that the significant improvement of NLO performance is attributed to the interface charge transfer and the optimization of absorption cross-sections in the ground and excited states. This work demonstrates the significance of the pore environment for NLO performance and provides an effective method for designing excellent NLO materials.

## Author contributions

H. H. Hou and J. Wu conceived and designed the research. K. S. Geng and Y. Wei performed the synthesis and characterization. K. S. Geng, Y. P. Sun, and J. Huang helped with the laser experiments. All authors contributed to the discussion and approved the final version of the manuscript.

## Conflicts of interest

The authors declare no conflict of interest.

## Data availability

Data available on request from the authors.

The data supporting this article have been included as part of the SI. Experimental details, PXRD, UV-vis spectra, FT-IR spectra, N<sub>2</sub> adsorption isotherms, HR-TEM, Z-scan figures, transient absorption, and DFT calculation. See DOI: <https://doi.org/10.1039/d5sc04193g>.

## Acknowledgements

This work was supported by the National Natural Science Foundation of China (No. 22171247 and 22471243).

## Notes and references

- (a) X. Zhao, P. Pachfule and A. Thomas, *Chem. Soc. Rev.*, 2021, **50**, 6871; (b) R. Liu, K. T. Tan, Y. Gong, Y. Chen, Z. Li, S. Xie, T. He, Z. Lu, H. Yang and D. Jiang, *Chem. Soc. Rev.*, 2021, **50**, 120; (c) Z. Lin, S. Dai, S. Yao, Q. Lin, M. Fu, L. Chung, B. Han and J. He, *Chem. Sci.*, 2025, **16**, 1948.
- Z. Wang, Y. Zhang, T. Wang, E. Lin, Y. Chen, P. Cheng and Z. Zhang, *Small*, 2023, **19**, 2303684.
- (a) Y. Zhang, J. Guo, P. Vannatta, Y. Jiang, J. Phipps, R. Roknuzzaman, H. Rabaa, K. Tan, T. Alshahrani and S. Ma, *J. Am. Chem. Soc.*, 2024, **146**, 979; (b) Z. Shao, J. Chen, Q. Xie and L. Mi, *Coord. Chem. Rev.*, 2023, **486**, 215118.
- A. Khojastegi, A. Khosropour, S. Amirjalayer, I. Mosleh and A. Abbaspourrad, *Adv. Funct. Mater.*, 2024, **34**, 2309367.
- (a) Y. D. Fang, Y. X. Liu, H. J. Huang, J. Z. Sun, J. X. Hong, F. Zhang, X. F. Wei, W. Q. Gao, M. C. Shao, Y. L. Guo, Q. X. Tang and Y. Q. Liu, *Nat. Commun.*, 2024, **15**, 4856; (b) Y. J. He, Y. Zhao, X. F. Wang, Z. Y. Liu, Y. Yu and L. Y. Li, *Angew. Chem., Int. Ed.*, 2023, **62**, e202307160.
- B. P. Biswal, S. Valligatla, M. Wang, T. Banerjee, N. A. Saad, B. M. K. Mariserla, N. Chandrasekhar, D. Becker, M. Addicoat, I. Senkovska, R. Berger, D. N. Rao, S. Kaskel and X. Feng, *Angew. Chem., Int. Ed.*, 2019, **58**, 6896.
- (a) A. Dey, S. Chakraborty, A. Singh, F. A. Rahimi, S. Biswas, T. Mandal and T. K. Maji, *Angew. Chem., Int. Ed.*, 2024, **63**, e202403093; (b) T. X. Luan, L. B. Xing, N. Lu, X. L. Li, S. Kong, W. W. Yu, P. Z. Li and Y. L. Zhao, *J. Am. Chem. Soc.*, 2025, **147**, 12704.
- (a) L. Grunenberg, G. Savasci, S. T. Emmerling, F. Heck, S. Bette, A. C. Bergesch, C. Ochsenfeld and B. V. Lotsch, *J. Am. Chem. Soc.*, 2023, **145**, 13241; (b) B. Q. Yu, R. B. Lin, G. Xu, Z. H. Fu, H. Wu, W. Zhou, S. F. Lu, Q. W. Li, Y. C. Jin, J. H. Li, Z. G. Zhang, H. L. Wang, Z. R. Yan, X. L. Liu, K. Wang, B. L. Chen and J. Z. Jiang, *Nat. Chem.*, 2024, **16**, 114.
- (a) M. C. Guo, X. Y. Guan, Q. Q. Meng, M. L. Gao, Q. X. Li and H. L. Jiang, *Angew. Chem., Int. Ed.*, 2024, **63**, e202410097; (b) Y. Teng, J. Zhao, Z. M. Ye, C. W. Tan, L. L. Ning, Y. Y. Zhou, Z. L. Wu, D. B. Kuang and Y. J. Li, *Adv. Energy Mater.*, 2025, **15**, 2404029.
- (a) A. S. Altowyan, G. Jagannath, K. Keshavamurthy and M. I. Sayyed, *Inorg. Chem. Commun.*, 2023, **155**, 110991; (b) M. Ashraf, M. S. Ahmad, Y. Inomata, N. Ullah, M. N. Tahir and T. Kida, *Coord. Chem. Rev.*, 2023, **476**, 214928; (c) R. Saha, B. Mondal and P. S. Mukherjee, *Chem. Rev.*, 2022, **122**, 12244.
- (a) E. K. Fox, F. El Haddassi, J. Hierrezuelo, T. Ninjbadgar, J. K. Stolarczyk, J. Merlin and D. F. Brougham, *Small*, 2018, **14**, 1802278; (b) Q. Q. Guan, C. W. Zhu, Y. Lin, E. I. Vovk, X. H. Zhou, Y. Yang, H. C. Yu, L. N. Cao, H. W. Wang, X. H. Zhang, X. Y. Liu, M. K. Zhang, S. Q. Wei, W. X. Li and J. L. Lu, *Nat. Catal.*, 2021, **4**, 840; (c) Z. H. Yan, M. G. Taylor, A. Mascareno and G. Mpourmpakis, *Nano Lett.*, 2018, **18**, 2696.
- (a) Y. Deng, Z. Zhang, P. Y. Du, X. M. Ning, Y. Wang, D. X. Zhang, J. Liu, S. T. Zhang and X. Q. Lu, *Angew. Chem., Int. Ed.*, 2020, **59**, 6082; (b) Y. M. Huang, P. Y. Du, W. X. Shi, Y. Wang, S. Yao, Z. M. Zhang, T. B. Lu and X. Q. Lu, *Appl. Catal., B*, 2021, **288**, 120001.
- (a) Y. Liu, L. Li, H. Tan, N. Ye, Y. Gu, S. Zhao, S. Zhang, M. Luo and S. Guo, *J. Am. Chem. Soc.*, 2023, **145**, 19877; (b) Y. J. Zhao, Z. C. Shao, Y. Cui, K. S. Geng, X. R. Meng, J. Wu and H. W. Hou, *Small*, 2023, **19**, 2300398.
- (a) H. Y. Liu, Y. Zhou, J. B. Guo, R. Feng, G. L. Hu, J. D. Pang, Y. Chen, O. Terasaki and X. H. Bu, *J. Am. Chem. Soc.*, 2023, **145**, 23227; (b) Y. M. Liu, Q. Zhou, H. D. Yu, Q. Q. Yang, M. C. Wang, C. H. Huang, L. X. Xiang, C. Li, T. Heine, G. Q. Hu, S. Y. Wang, X. L. Feng and Y. Y. Mai, *Angew. Chem., Int. Ed.*, 2024, **63**, e202400985.



- 15 Y. Jiao, Q. Lian, Z. Li, M. Lin, D. Ma, Z. Tang, D. Xia and M. Zhu, *Adv. Funct. Mater.*, 2025, 2500501.
- 16 K. Geng, T. He, R. Liu, S. Dalapati, K. T. Tan, Z. Li, S. Tao, Y. Gong, Q. Jiang and D. Jiang, *Chem. Rev.*, 2020, **120**, 8814.
- 17 (a) Y. Cui, Y. J. Zhao, J. Wu and H. W. Hou, *Nano Today*, 2023, **52**, 101972; (b) Y. Cui, Y. J. Zhao, J. Wu and H. W. Hou, *Adv. Funct. Mater.*, 2023, **33**, 2302573.
- 18 W. A. Spieker, J. Liu, J. T. Miller, A. J. Kropf and J. R. Regalbuto, *Appl. Catal., A*, 2002, **232**, 219.
- 19 (a) R. J. Wei, M. Xie, R. Q. Xia, J. Chen, H. J. Hu, G. H. Ning and D. Li, *J. Am. Chem. Soc.*, 2023, **145**, 22720; (b) D. L. Zhang, Y. H. Zhu, L. M. Liu, X. R. Ying, C. E. Hsiung, R. Sougrat, K. Li and Y. Han, *Science*, 2018, **359**, 675; (c) Y. Tong, L. Yu, N. Li, M. Shen, X. Peng, H. Yang, Y. Ye, F. Zhu, J. Pawliszyn, J. Xu and G. Ouyang, *Chem. Sci.*, 2022, **13**, 13948.
- 20 (a) E. Avila, H. Salway, E. Ruggeri, C. Camur, N. Rampal, T. A. S. Doherty, O. D. I. Moseley, S. D. Stranks, D. Fairen-Jimenez and M. Anaya, *Matter*, 2024, **7**, 4319; (b) Y. J. Zhao, Y. Cui, X. R. Meng, J. Ding and H. W. Hou, *Coord. Chem. Rev.*, 2022, **473**, 214815.
- 21 (a) M. M. Gao, J. F. Kou, M. H. Xu, K. Yuan, M. Y. Li and Z. P. Dong, *Green Chem.*, 2024, **26**, 3884; (b) M. E. Silva, M. O. Palm, D. A. Duarte and R. C. Catapan, *ACS Omega*, 2023, **8**, 6507.
- 22 W. Shi, B. S. Zhang, Y. M. Lin, Q. Wang, Q. Zhang and D. S. Su, *ACS Catal.*, 2016, **6**, 7844.
- 23 D. Zhao, C.-L. Dong, W. Bin, C. Chen, Y.-C. Huang, Z. Diao, S. Li, L. Guo and S. Shen, *Adv. Mater.*, 2019, **31**, 1903545.
- 24 Z. H. Guan, L. L. Fu, L. Chen, Z. Y. Wei, F. Liu, Y. Zhao, Z. P. Huang, M. G. Humphrey and C. Zhang, *Chem. Sci.*, 2025, **16**, 6720.
- 25 K. S. Geng, Y. P. Sun, Y. J. Zhao, Z. C. Shao, Y. Wei, J. Huang, Y. Cui, X. Y. Xu and H. W. Hou, *J. Am. Chem. Soc.*, 2025, **147**, 9844.
- 26 M. Priyadarshini, J. N. Acharyya, S. Mahajan and G. V. Prakash, *Opt. Laser Technol.*, 2021, **139**, 107008.
- 27 N. Shan, Z. Wei, Z. Guan, Y. Zhao, F. Liu, L. Fu, Y. Xue, Z. Huang, M. G. Humphrey, J. Xu and C. Zhang, *J. Mater. Chem. C*, 2023, **11**, 16708.
- 28 (a) Y. P. Sun, W. J. Xu, F. F. Lang, H. R. Wang, F. F. Pan and H. W. Hou, *Small*, 2024, **20**, 2305879; (b) M. Lv, X. Wu, W. Wang, D. Han, S. Chen, Y. Hu, Q. Zhang, Q. Wang and R. Wei, *ACS Sens.*, 2025, **10**, 1778.
- 29 B. S. Kalanoor, L. Gouda, R. Gottesman, S. Tirosh, E. Haltzi, A. Zaban and Y. R. Tischler, *ACS Photonics*, 2016, **3**, 361.
- 30 H. Li, S. Y. Chen, D. W. Boukhvalov, Z. Y. Yu, M. G. Humphrey, Z. P. Huang and C. Zhang, *ACS Nano*, 2022, **16**, 394.
- 31 (a) Z. T. Zhang, Q. Q. Yang, X. J. Zhen, Z. Z. Feng, X. P. Zhai, X. D. Zhang, Y. F. Huang, Q. Wang and H. L. Zhang, *ACS Appl. Mater. Interfaces*, 2021, **13**, 21626; (b) M. Y. Li, C. T. Gong, J. W. Du, D. B. Ding, D. D. Du, D. F. Wang, J. R. Jiang, T. T. Li, C. Zheng, Y. F. Yang, Y. B. She and J. H. Jia, *ACS Mater. Lett.*, 2023, **5**, 694.
- 32 (a) M. J. Diao, H. Li, X. Y. Gao, R. P. Hou, Q. Cheng, Z. Y. Yu, Z. P. Huang and C. Zhang, *Adv. Funct. Mater.*, 2021, **31**, 2106930; (b) H. Li, M. J. Diao, D. W. Boukhvalov, Y. T. Ke, M. G. Humphrey, C. Zhang and Z. P. Huang, *Adv. Funct. Mater.*, 2024, **34**, 2400077.
- 33 (a) D. J. Li, Q. H. Li, Z. R. Wang, Z. Z. Ma, Z. G. Gu and J. Zhang, *J. Am. Chem. Soc.*, 2021, **143**, 17162; (b) Z. Z. Ma, Q. H. Li, Z. R. Wang, Z. G. Gu and J. Zhang, *Nat. Commun.*, 2022, **13**, 6347; (c) J. Sun, X. K. Tang, Z. H. Liu, Z. L. Xie, B. Z. Yan, R. F. Yin, C. Chaolumen, J. Zhang, W. H. Fang, J. Y. Wei and H. Shen, *ACS Mater. Lett.*, 2024, **6**, 281.
- 34 (a) J. Chakraborty, A. Chatterjee, K. Molken, I. Nath, D. A. Esteban, L. Bourda, G. Watson, C. H. Liu, D. Van Thourhout, S. Bals, P. Geiregat and P. Van der Voort, *Adv. Mater.*, 2024, **36**, 2314056; (b) B. Han, B. Liang, E. H. Zhang, J. Li, Y. F. Li, Q. Zhang, Z. Xie, H. L. Wang and J. Z. Jiang, *Adv. Funct. Mater.*, 2024, **34**, 2404289.
- 35 B. Li, H. Li, C. Wu, L. Fu, D. W. Boukhvalov, M. G. Humphrey, C. Zhang and Z. Huang, *Angew. Chem., Int. Ed.*, 2024, **63**, e202406941.

